LAUNCH CANADA 2025 PAYLOAD CHALLENGE

Final Payload Design Report for Aurora

Competing Team 24 - Waterloo Rocketry

TABLE OF CONTENTS

LIST OF FIGURES

LIST OF TABLES

1 PAYLOAD

1.1 Payload Experiment

A mid-infrared (MID-IR) Fourier-transform spectrometer was chosen as the payload experiment for this design cycle. Its purpose is to monitor the wavelengths of infrared light being transmitted and absorbed through the troposphere to identify the presence of greenhouse gases by comparing experimental results with known absorption spectra. Specifically, due to the range of infrared light this spectrometer can detect, this experiment aims to remotely sense levels of carbon dioxide (CO_2), nitrous oxide (N_2O), and methane (CH_4) concentrations in the troposphere.

1.1.1 Experiment Background

Fourier transform spectroscopy, commonly known as FTIR spectroscopy when used with infrared light, is a technique for extracting information from electromagnetic (EM) radiation. Fundamentally, this technique utilizes the superposition of EM waves to vary the intensity of light measured, which can then be mathematically related to the absorption of light through a Fourier transform [1].

Since this relies so heavily on interference, the core of an FTIR spectrometer is some variation of an interferometer, most often a Michelson interferometer much like the one shown in Figure 1.2.

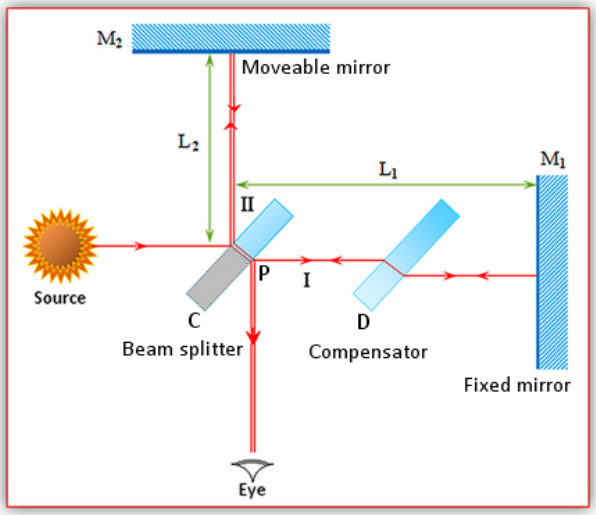

Figure 1.1: A Michelson interferometer [2]

The Michelson interferometer has five main components. These are a beamsplitter, a compensator, a fixed mirror, an adjustable mirror, and a system for observation, such as a sensor, telescope, or screen. The working principle is best explained by following the light's path. Upon entering the spectrometer, the incident beam strikes the beamsplitter with its coating facing towards the light at a 45 degree angle. This produces two separate but identical beams of light travelling perpendicular to each other. The first beam reflects off the beamsplitter coating without refracting. It travels towards a mirror with an adjustable path length where it is reflected back towards the beamsplitter. Once it reaches the beamsplitter again, it is refracted once and transmitted towards the sensor.

The second beam is initially refracted and transmitted through the beamsplitter. It travels towards a mirror with a fixed path length before being reflected back towards the beamsplitter. Once it reaches the beamsplitter again, it is refracted a second time and reflected towards the sensor. An uncoated compensator of the same thickness and material as the beamsplitter is added between the fixed mirror and the beamsplitter to account for and undo the effects of the second refraction of the beam [3]. At this point, both beams of light are travelling towards the sensor, where their interference patterns are observed.

By having an adjustable mirror, a difference in the path lengths of the two identical beams can be created. This path difference causes constituent wavelengths to interfere constructively or destructively differently at specific points. This interference allows precise measurements of the wavelengths of light that are present [4]. FTIR spectrometers collect intensity over mirror position, producing interferograms. These interferograms can be Fourier transformed using a discretized algorithm based on the Fourier-transform equation presented by Saptari, shown in Equation 1.1 [4].

$$F(\nu) = \int_{-\infty}^{\infty} e^{-2\pi i \nu x}\, dx \tag{1.1}$$

Where

x = position
ν = wave number
e = Euler's number

By discretizing the equation, the integral can be given definite bounds and can be efficiently computed. This algorithm is known as the Discrete Fourier Transform (DFT), which is the basis of the much faster Fast Fourier Transform (FFT) [5]. This algorithm transforms the modulated intensity data in the interferogram from the mirror position domain into the wave number domain, meaning that the interferogram is now a spectrum and represents the transmittance/absorption of light against wave number [4]. The dips in transmittance in this spectrum can be compared to reference data from organizations such as the National Institute of Standards and Technology (NIST) and correlated to gases and compounds in the atmosphere that absorb that light, showing that the specific gas is between the spectrometer and the light source. For instance, nitrous oxide absorbs over 99.9% of light around 4.45-4.55 μm, so detecting a dip in this range is indicative of nitrous oxide presence [6].

1.2 Experiment Methodology

The relevant raw data from the spectrometer consists of the interferograms displaying signal intensity compared to the difference in path length. The signal intensity is recorded in volts, while the path difference is recorded in nm. Applying the FFT to this data results in a signal intensity spectrum in the wave number domain, where wave number is defined by Equation 1.2.

$$\nu = \frac{1}{\lambda} \tag{1.2}$$

Where

ν = wave number

λ = wavelength

To compare with traditional Fourier transforms from the time domain to the frequency domain, recording a change in path difference is analogous to recording a change in time, and the wave number spectrum is analogous to the frequency spectrum.

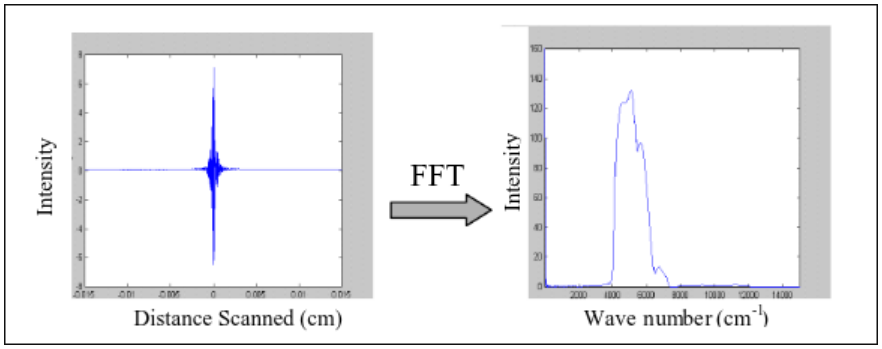

Figure 1.2: An example transformation into the wave number domain [4]

This spectrum can be normalized by comparing experimental intensity values at each wave number to their expected intensity values based on the blackbody emission spectra of the Earth and the Sun. These expected values can be calculated using Planck's Radiation Law, described in Equation 1.3.

$$I(\nu, T) = \frac{8\pi\nu^2}{c^5} \cdot \frac{h\nu}{e^{\frac{h\nu}{kT}} - 1} \tag{1.3}$$

Where

I = radiative intensity

ν = wave number of radiation

T = temperature of the blackbody

h = Planck's constant

k = Boltzmann's constant

e = Euler's number

The normalized absorption values can then be compared to known absorption spectra to determine the concentration of detected greenhouse gases.

1.2.1 Spectrometer Design

The selected optics are made and sold by Thorlabs and are specialized for the mid-to-near infrared range. These consist of the following:

- A half-inch diameter, 3 mm thick CaF_2 beam splitter optimized for the $2-8\,\mu$m wavelength band with reflectance ranging from 40-65% and transmittance ranging from 35-60% in the $2-5\,\mu$m band [7].
- A half-inch CaF_2 compensator of the same thickness (3 mm) with 94-96% transmittance [8].
- Two half-inch diameter protected gold mirrors with reflectance around 90-97% [9].
- A CaF_2 plano-convex lens will focus the incoming light onto the very small active area of the sensor. It is half-inch diameter, with a focal length of 20 mm. The paraxial ray approximation (light rays from distant sources are approximately parallel to each other) is used for the incoming light, thus a plano-convex lens should focus the incoming light well. It is 4.3 mm thick at its widest, with an average of 96% transmittance in the $2-5\,\mu$m range [10].

The other components of the spectrometer are a Hamamatsu P13243-011MA infrared detector, a 5 V continuous rotation servo, and a micrometer screw. The optical components are responsible for defining the light path and directing it onto the Hamamatsu detector, which produces a current proportional to the intensity of the light. To modulate the interference, one of two mirrors is linked to the micrometer screw, which is attached to the servo. Using micrometer screws for accurate positioning is common in Michelson interferometers, as they can easily change rotation to linear motion and have high precision. The assembly is about 5.7 x 3.7 x 5.5 in (length, width, height) in CAD. A cross-section view is shown below in Figure 1.3.

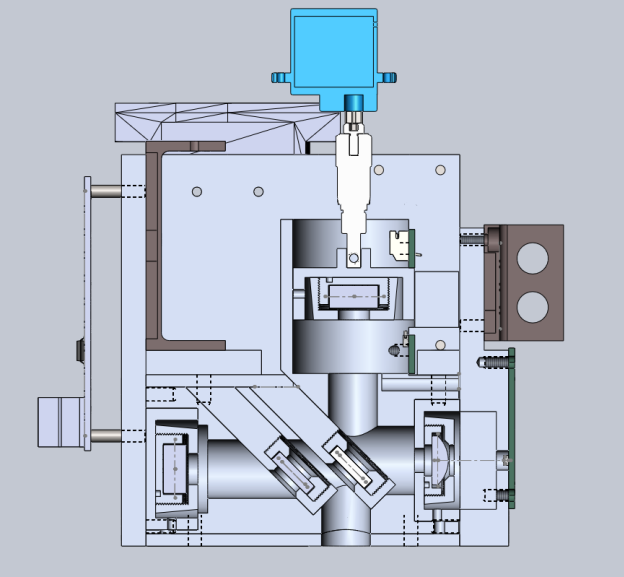

Figure 1.3: Spectrometer cross-Section

Many design choices for the assembly are inspired by the designs outlined by Yoder[11]. Namely, conical lens holders with radial set screws for adjustability were featured in Chapter 2.1.2, and calculations for the custom 0.7 in 40 TPI thread FOS from Chapter 3.4 were used. In this design, one part sets the spacing and placement of all optical components to avoid stacked tolerances causing differing path lengths. Additionally, the optic holders along with the non-standard 40 TPI

thread used for retention allow for fine adjustment of optic positions. This was chosen instead of a more traditional poker chip assembly since the likelihood of being within the very tight tolerances demanded by optical assemblies was very low, so adjustability is a countermeasure. While not shown in this cross-section, there are Buna-N gaskets placed on the faces of the assembly that the optics contact. An example of one of these mounting faces with a gasket is shown in Figure 1.4 These act to avoid scratching the optics, increase friction to avoid parts sliding, and act as vibration dampers.

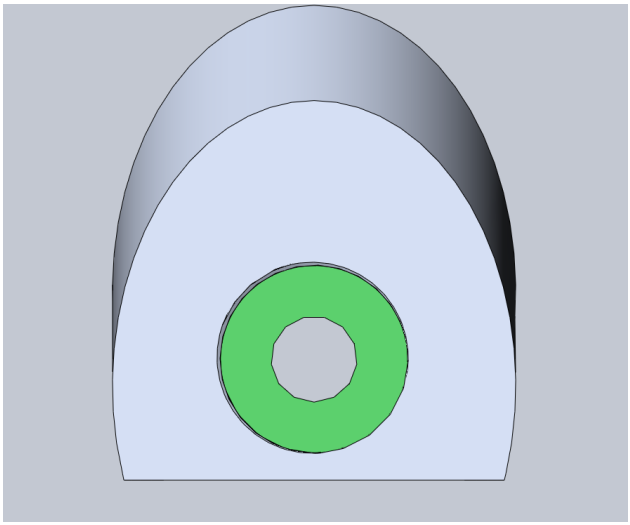

Figure 1.4: An example optic mounting face

A slightly outdated design of the light path was simulated in the holders using Ansys Zemax OpticStudio to confirm that light could travel through the entirety of the section and that the light would be focused on the sensor. This light path is still representative of the flight configuration.

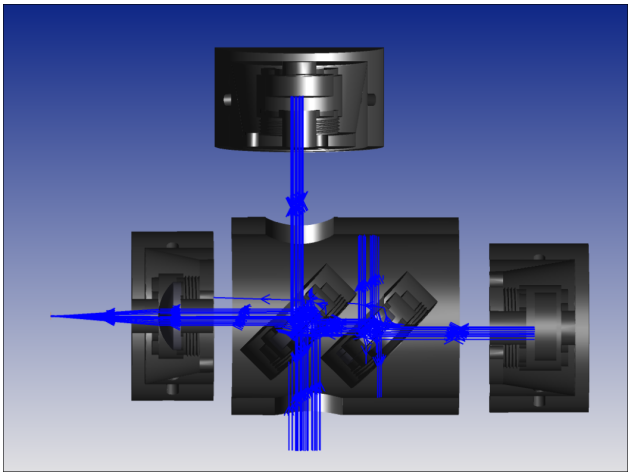

Figure 1.5: Ansys Zemax OpticStudio simulation

These results confirm that the light reaches the sensor in focus, and the final position of all optics was based on fine tuning performed in these simulations.

1.3 Payload Electrical Architecture

Due to the complete separation from the flight vehicle, the payload must function independently from all other avionics. Furthermore, the spectrometer requires multiple electronic components to produce useful data. The payload therefore contains seven custom-designed PCBs and two COTS altimeters: copies of Power Board, Motor Control Board (not to be confused with the canards motor control board), Sensor Board, Camera Board, Remote Arming, two Limit Boards, a Featherweight Raven2, and a Perfectflite StratologgerCF. Additionally, a 70 cm Big Red Bee GPS transmitter is housed in the nosecone with its own 850 mAh battery for post-flight tracking and retrieval. The architecture of these boards is shown in Figure 1.6. The details of each board follow.

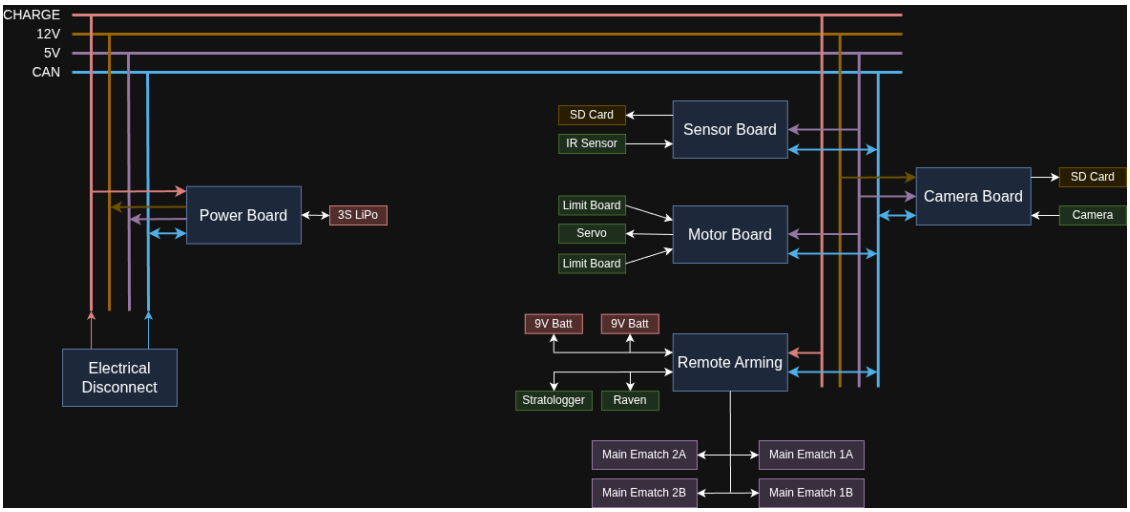

Figure 1.6: Payload electrical architecture

1.3.1 Payload Sensor Board

The sensor board is the heart of the experiment and is responsible for reading the infrared light intensity sensor and logging the messages of all the other boards for post-processing.

- The P13243-013CA Hamamatsu sensor is sensitive to light in the $2 - 5\,\mu$m band and due to the material and design of the semiconductor, converts incident photons to moving electrons. This means that light intensity is proportional to the produced current. This current is normally around 100 nA to 1 μA, so a transimpedance amplifier is used to convert the photocurrent to a voltage that is read by an analog-to-digital converter (ADC).
- A micro-SD card holder is soldered onto this board. This logs all the messages of the payload boards for post-processing the flight. Placing this SD card on this board is important because it can log the ADC samples of the sensor at the high sample frequency, which would otherwise clog all communication between boards. This relatively high sample rate also means more precise wavelength measurements after the Fourier transform, so this speed is too important of a factor to use previously existing boards to log the information.

- To effectively scan the entire wavelength spectrum with the desired resolution, the ADC must be sampled thousands of times per second. To do this, a dedicated ADC IC is used on the board instead of the PIC18s. This provides a means to sample at the desired 15 kHz and limits noise. Additionally, this ADC is 24-bit for a compromise on precision and price. The PIC18 communicates with this ADC via SPI and logs the data directly to the micro-SD card.
- Due to concerns about random noise being larger than the produced photocurrents, several features were added to this board to avoid noise contamination. It is a 4-copper-layer board, with analog and digital grounds separated and poured on different layers. Furthermore, the placement of the sensor was such that it avoided noisy components such as the oscillator, which was also shielded by vias.

1.3.2 Payload Limit Board

Two of these will be flown, and used to reverse the servo's direction of rotation.

- Each board has a limit switch and a JST connector on them connected to the motor board.
- These limit boards define the top and bottom of the mirror path by connecting the 5V input pin of the JST to the output pin when the mirror presses the switch. This output is wired into one of the PIC18 pins so the change in voltage can be read and used to change direction.

1.3.3 Payload Motor Board

The motor board controls the servo that moves the mirror causing the path difference.

- The board sends pulse width modulated (PWM) signals to a FITEC FS90R continuous rotation servo. These signals switch the servo on and off typically every millisecond or two to control the direction and speed of rotation.
- The servo direction is determined by the limit switches mounted on the limit boards.

1.3.4 Altimeters

The altimeters are responsible for igniting the black powder in the recovery components. Altitude is determined by barometric pressure in the case of the Stratologger, and a fusion of accelerometer and barometric data for the Raven2. These altimeters have been flight validated in the May test launch, which resulted in a nominally recovery with the configurations shown in Figure 1.7 and Figure 1.8. For the Aurora flight these configurations are identical, however the main parachute is programmed to deploy at 5000, These altimeters are initally armed through a Featherweight MagSwitch, and can be armed and disarmed later via CAN messages to Remote Arming. When the deployment criteria are met, the altimeters send current from each of their dedicated 9V batteries into the screw terminals located on the top bulkhead. One of two e-matches from the two pyrocutters and the two CO_2 ejectors is wired to these terminals, and therefore fire when this occurs. This system is entirely dually redundant in compliance with the DTEG requirement 9.3.1. There are two independent altimeters which operate based on different mechanisms, each with their own battery, and each wired to one of two e-matches in each of the two pyrocutters and two CO_2 ejectors.

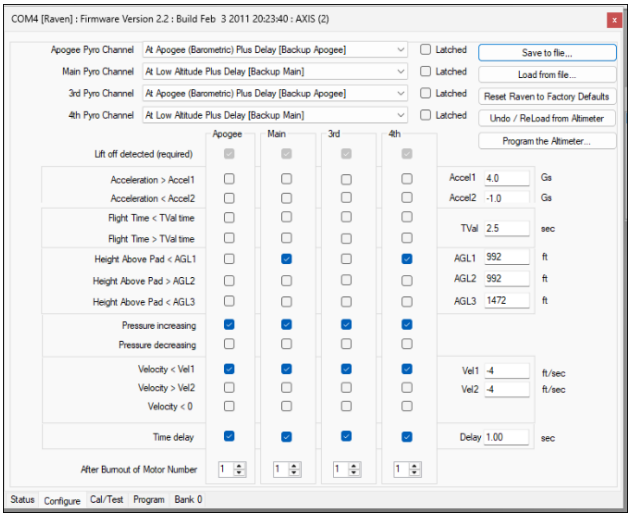

Figure 1.7: Raven2 configuration for the test flight.

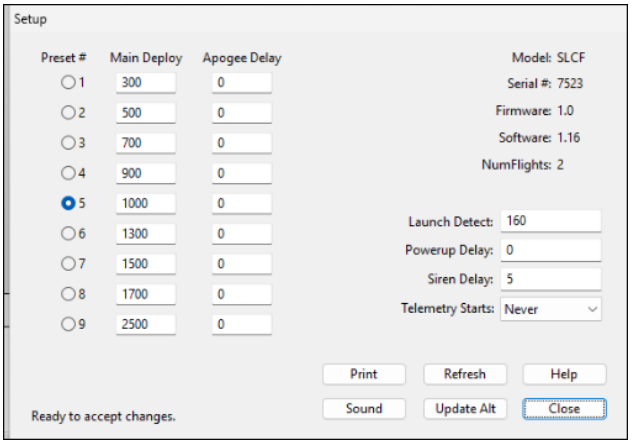

Figure 1.8: StratologgerCF configuration for the test flight.

1.3.5 Common Electronics

The other boards, specifically the Power Board and Camera Board are detailed in Section 9 of the main vehicle report, while Remote Arming is detailed in Section 10 [12].

1.3.6 Electrical Testing

Electrical testing for the system includes individual testing of boards, benchtop tests of the whole system, harnessing/assembly tests, and vacuum testing. Individual testing serves to validate each boards individual functions, for instance reading the IR sensor or charging the LiPo. The benchtop test serves to trouble shoot integration problems, such as power cycling. Harnessing tests are important for validating the rigidity and length of connections will not be a failure mode and gives practice assembling the entire system. The last set of testing is vacuum chamber testing of the altimeters. While the Raven2 Firmware Interface Program (FIP) can run simulated flights to validate altimeter triggers, the Stratologger cannot. However, since it is purely barometric, pulling

vacuum around the Stratologger acts as a simulated flight and can be used to verify the altimeter is working as intended.

1.4 Deployable Payload Recovery System

To reach the desired environmental conditions for this year's experiment, an independent recovery system was designed for the nosecone to allow the payload to deploy and descend separately from the main rocket body. This occurs in two stages. The first is a flat-spin descent, experimentally determined to have a terminal velocity of 150 ft/s below 6000 ft. The second is descent under main parachute, experimentally determined to reach a terminal velocity of 27 ft/s at sea level. Dispersion analysis has been performed for this system by the Waterloo Rocketry Flight Dynamics subsystem [12], and the system has been demonstrated to be functional through a fully representative test flight.

1.4.1 Sequence and Events Summary

The initial separation of the nosecone-payload assembly occurs at apogee, when the main rocket recovery system pressurizes the section below the nosecone to break the joint shear pins and push the nosecone off. From this point on, a single-separation single-deployment sequence is utilized to recover this assembly. Prior to main deployment, the nosecone descends independently in a flat spin descent. The payload is retaining in the nosecone for the entirety of the flat spin descent with the use of suspension lines attached to an eyebolt in the nosecone tip. Once the packed system reaches 5 000 ft, the retaining lines are cut using SRAD line cutters and the payload sled is pushed out of the nosecone using pressure from two 20 g CO_2 charges. The main chute bag and pilot chutes that are stored closer to the nosecone tip follow. The pilot chute then extends the shock cord and suspension lines before pulling the main chute out of its packed configuration in the bag, creating a lines first deployment sequence.

1.4.2 Experiment Sled

The main experiment sled is shown in Figure 1.9. The main structure consists of two bulkheads connected by three 6 *in* longerons, all machined from 6061-T6 aluminum. These longerons all have a FOS over 30, which was calculated the same way as the injector section longerons detailed in Section 7 of the main vehicle report [12]. During flight, the experiment sled resides in a 3D-printed cylindrical sheath that is bonded into the nosecone. O-rings were utilized on both bulkheads to create a sealed environment above and below the experiment sled. This was to allow for pressurization of the sections above and below the payload throughout flight. The payload experiment and all electrical hardware mounts to the lower bulkhead, where an aperture was created to allow light to pass to the spectrometer. The retainment and deployment mechanisms mount to the upper bulkhead, which is shown in Figure 1.10. More detail on these mechanisms will be provided in subsubsection 1.4.6 and subsubsection 1.5.1 respectively.

1.4.3 Flat Spin Descent

Inspired by the conceptual mission designed by the University of Arizona Fairbanks [13], the nosecone-payload packed assembly was designed to enter a flat spin during free fall to decrease

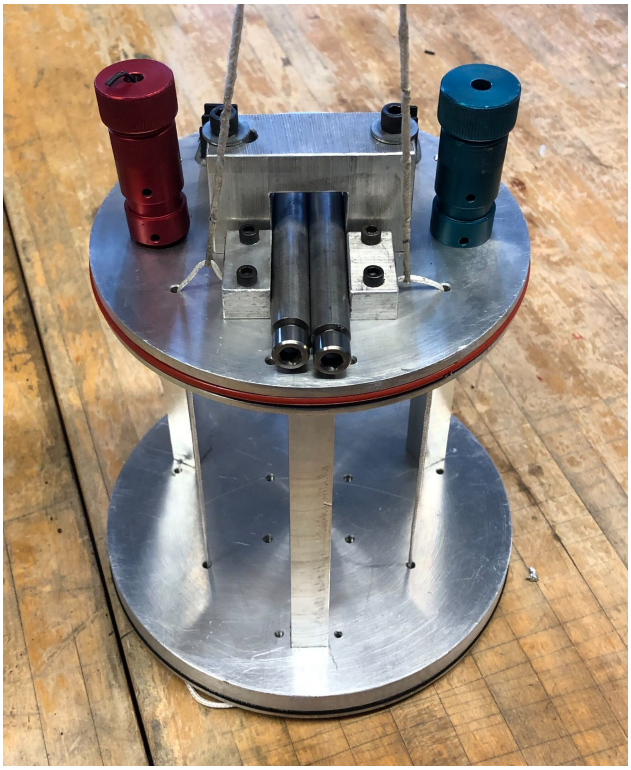

Figure 1.9: Payload experiment sled

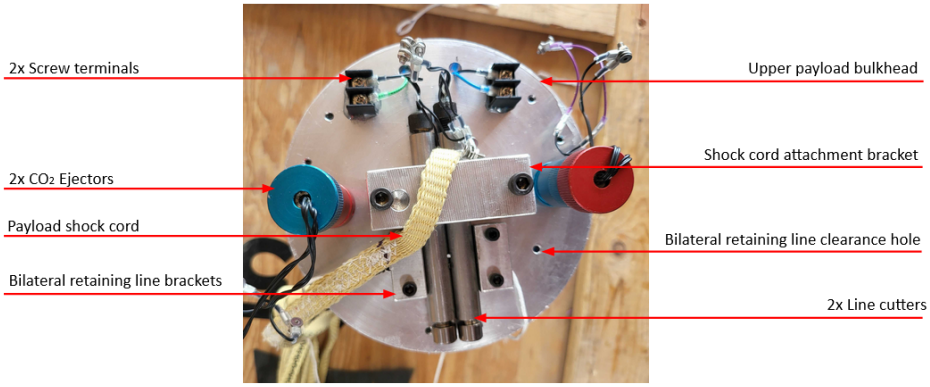

Figure 1.10: Payload upper bulkhead mechanical components

terminal velocity. This was done by balancing the centre of gravity (C_g) and centre of pressure (C_p) such that the C_g was closer than the C_p was to the base of the cone. This prevents the undesirable outcome of the nosecone tip pointing in the direction of motion, which would lower the assembly C_d due to the aerodynamics of the nosecone in this orientation. It was difficult to predict how flat the nosecone would be in descent without experimental data, however test flight launched in May 2025 provided confirmation that the spin was approximately parallel to the ground.

The test flight also showed that the terminal velocity of the nosecone-payload assembly in free fall was 150 ft/s, with a rotational frequency of approximately 1 Hz at 4 000 ft in medium speed winds.

1.4.4 Main Parachute

Canopy Design

The main payload parachute was chosen to be an SRAD cross type parachute. This was chosen for its stability, easy of fabrication, and good balance between opening force coefficient and C_d. The design follows the typical style illustrated by Knacke [14].

The width to length ratio was chosen to be 0.264 to provide a balance between stability and C_d; as the width to length ratio decreases, chute stability increases, but C_d decreases [15]. According to Knacke, drag coefficients for cross parachutes range from 0.60 to 0.85[14]. This was supported by a study performed by the University of Minnesota [15], which shows that for the width to length ratio of 0.264 and low porosity fabric, the corresponding C_d at an angle of attack of zero ranges from 0.79 to 0.84. A design C_d of 0.80 was used as a conservative value when sizing the required canopy area. Note that parachute sizing was done early in the design cycle, therefore the payload mass has changed slightly since these calculations were completed.

First, as illustrated in Knacke [14], the canopy area of a chute can be determined using dynamic pressure. This is described in Equation 1.4.

$$F_d = q \cdot S \cdot C_d \tag{1.4}$$

Where

F_d = drag force
q = dynamic pressure
S = total canopy area
C_d = coefficient of drag

Additionally, Knacke provides a relationship between dynamic pressure and velocity, shown in Equation 1.5.

$$q = \frac{1}{2} \cdot \rho \cdot v^2 \tag{1.5}$$

Where

v = air flow velocity

ρ = air density

For a terminal velocity of 27 ft/s at 5 000 ft, a drag coefficient of 0.80, and a predicted load of 14 lb, the following calculations were performed to determine a canopy area of 23.44 ft^2. The value for ρ is provided by Knacke [14].

$$
\begin{aligned}
v &= 27 \text{ ft/s} \\
\rho &= 0.00204817 \text{ slugs/ft}^3 \\
F_d &= 14 \text{ lb} \\
C_d &= 0.80 \\
S &= \frac{2 \cdot 14}{0.00204817 \cdot 27^2 \cdot 0.80} = 23.44 \text{ ft}^2
\end{aligned}
$$

For a cross parachute with this area and a width to length ratio of 0.264, the corresponding band length and width were 7.15 ft and 1.88 ft respectively. See Figure 1.11 for a dimensioned profile of the cross parachute.

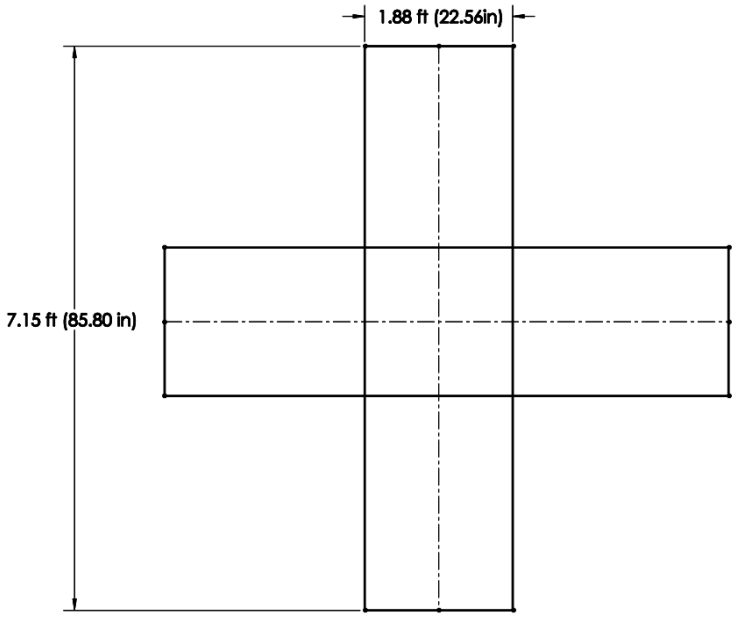

Figure 1.11: Dimensions and layout of sized cross parachute

The chosen canopy fabric was zero-porosity ripstop nylon, with nylon bias tape lining the perimeter and reinforcing suspension line connection points. Figure 1.12 shows the flat profile of the canopy; the black tapes are nylon bias tapes, and yellow and magenta fabrics are ripstop nylon.

Opening Force Loads

Theoretical calculations were done using the Pflanz method outlined by Knacke [14] to estimate loads caused by the inflation of the parachute. This resulted in a load of 155 lb at 5 000 ft. However, the test flight in May experimentally proved that the peak loads during chute inflation were closer to 324 lb (see subsubsection 1.5.3). This large discrepancy was likely caused by the additional energy from the deployment charges during the test flight. As the experimental load was higher than the theoretical load, the experimental load was considered to be the peak loading condition.

Figure 1.12: Fabric layout of main payload parachute

1.4.5 Harness, Interconnecting Hardware and Attachments

A diagram of the system rigging is shown in Figure 1.13.

Eight suspension lines were used, made from CYPRES AAD Loop material (CYPRES). Each CYPRES line is rated to over 400 lb, combining to withstand at minimum 3200 lb of loading. As discussed in subsubsection 1.4.4, the expected peak load on the suspension lines was determined to be about 324 lb. This provides a minimum factor of safety of almost ten. The suspension lines were sized to be equal in length to the main chute at 7.15 ft, as this was the convention followed in the study used to estimate parachute C_d. The inflated profile can be seen in Figure 1.14. The point of confluence is a quick link, connecting together all eight suspension lines and linking this assembly with the parachute shock cord.

The payload and parachute shock cords are identical in length and material. Both are 9.25 ft in length and made from Kevlar shock cord. This length was chosen to minimize material waste, as shortening it would result in material scraps that are too short for use in projects. The nosecone shock cord length is 6.17 ft in length. This was deliberately chosen to be shorter than the other two shock cords to prevent contact of the nosecone with the payload sled or the suspension lines post-deployment.

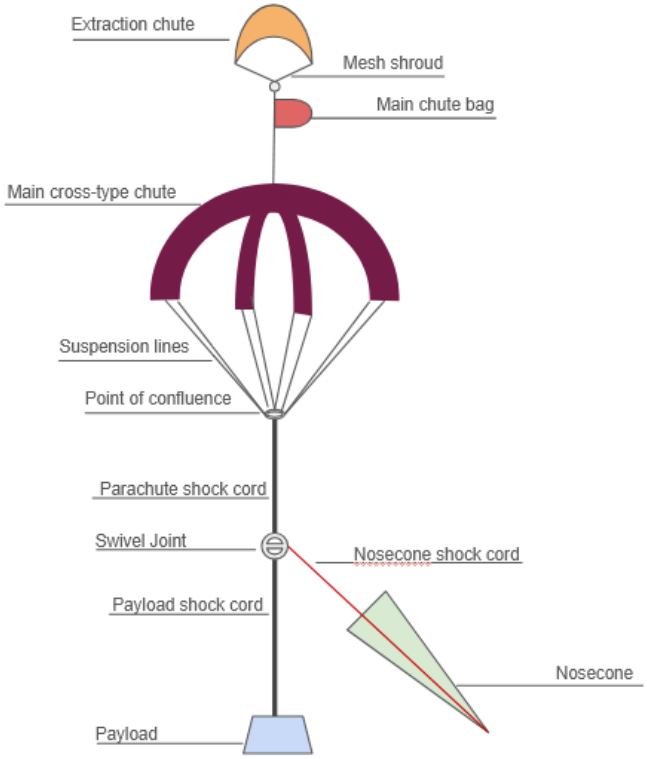

Figure 1.13: Rigging diagram of payload recovery system

Figure 1.14: Main payload parachute during truck test

A swivel joint was utilized to connect the three shock cords together, as shown in Figure 1.13. The goal of this was to prevent the wrapping of suspension lines as the cross type parachute spins, which would result in constriction of the canopy. Additionally, the swivel allows the nosecone to spin freely around the main shock cords without wrapping or pulling on the assembly.

The shock cord attaches to the payload sled via the shock cord attachment bracket. The bracket

is machined from 6061-T6 aluminum is secured to the upper bulkhead with the use of two 1/4-28 bolts. SolidWorks FEA was used to validate the ability of the bracket to withstand more than triple the expected peak loading conditions.

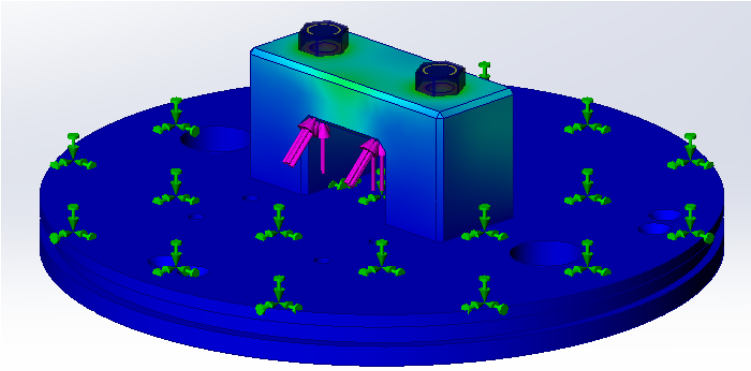

Figure 1.15: SolidWorks FEA performed on shock cord attachment bracket

Long distance drone footage from the test flight captured the deployed configuration of the recovery system. Figure 1.16 shows the pilot chute, main chute, experiment sled, and nosecone descending after deployment occurred.

Figure 1.16: Payload recovery system during the test flight

1.4.6 Retainment Mechanism

The payload sled is retained in the nosecone by the use of CYPRES lines. This consists of three lines total, two 'suspending lines' which extend from the nosecone eyebolt to the upper payload bulkhead, and one 'retaining line' that holds these lines in place. As shown in Figure 1.17, the retaining line passes through loops on the suspending lines, before passing underneath the retaining brackets and into the line cutters.

The cutouts in the retaining brackets are lower than the holes in the line cutters, pulling the line down on either side of the cutters (see Figure 1.18). The brackets themselves were machined from 6061-T6 aluminum and are secured to the bulkhead with the use of two #6-32 bolts each.

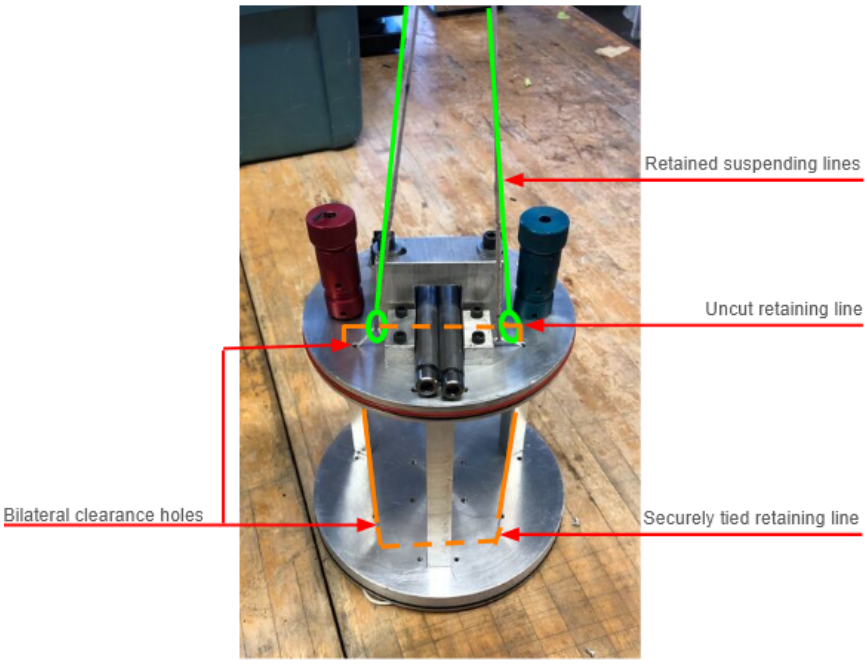

Figure 1.17: Retained payload system

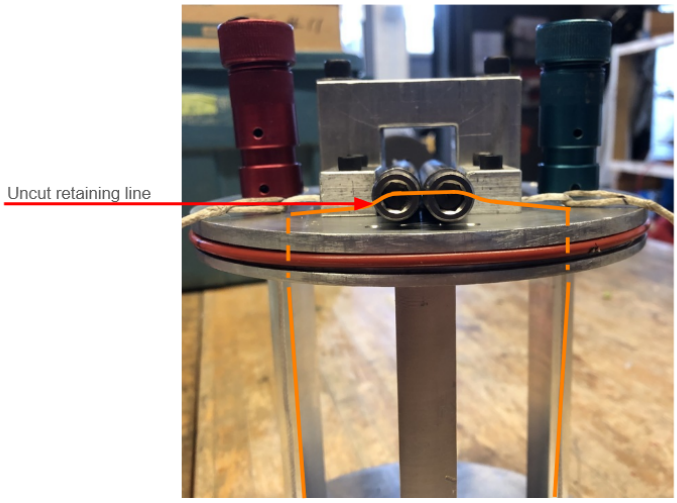

Figure 1.18: Retaining line path through retaining brackets and line cutters.

This prevents the line cutters from being dislodged by the retaining line, as any tension from the suspending lines will be redirected to pull the line cutters closer to the bulkhead. The retaining line then passes through clearance holes in both the upper and lower payload bulkheads and is permanently tightened at the base of the lower bulkhead.

The retaining line is the only line that need be cut to release the payload sled, as shown in Figure 1.19. This is done with the use of two stainless steel SRAD line cutters, creating a dual-redundant system as only one cutter must succeed for the system to function nominally. This line cutter design has been tested numerous times, including autonomous functionality tests and

integrated tests with the rest of the retainment system. All ground tests of these line cutters have shown nominal results, and this mechanism was therefore used on the test flight, where it again functioned nominally and successfully released the payload sled.

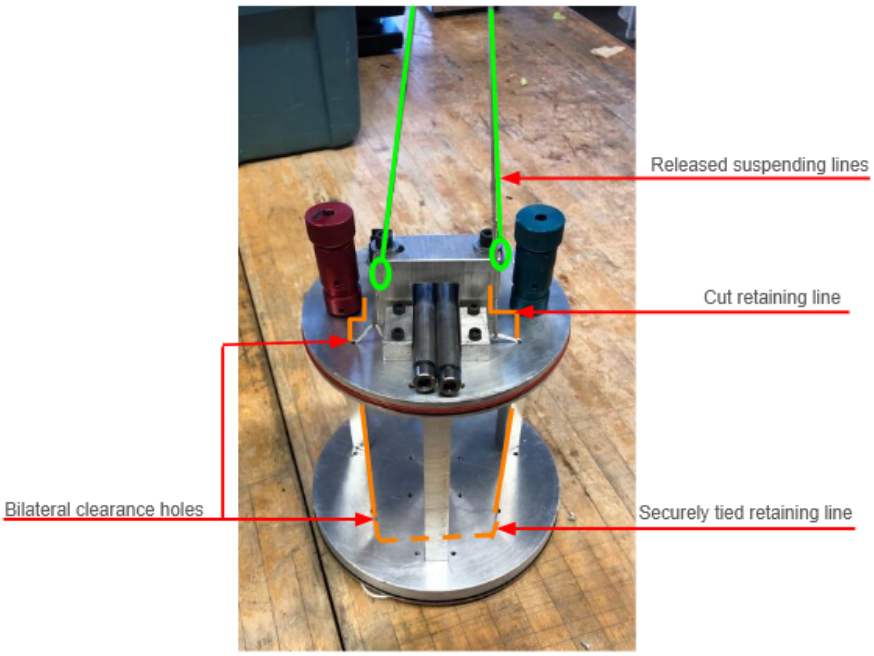

Figure 1.19: Released payload system

This method was chosen in favour of traditional methods such as shear pins to eliminate the need for deployment charges to break the retaining mechanism. As the payload resides in the nosecone, failure of the retaining mechanism was determined to be an unacceptable failure mode due to risk of interfering with the main rocket recovery system. By separating the processes of releasing and deploying the payload, it was made possible to create a stronger retaining system without increasing the amount of energetic required to deploy the system.

1.4.7 Deployment Mechanism

Two 20 g CO_2 canisters, punctured with COTS CO_2 ejectors, were chosen to pressurize the upper section of the nosecone and deploy the payload sled. Only one of these canisters must successfully discharge to deploy the payload sled.

1.5 Testing

A series of tests were performed to validate the performance of the payload subsystem. Most notable was a test flight launch in May of 2025, which provided a full test of the full recovery system. Details on this test and others performed are as follows.

1.5.1 Deployment Tests

These tests were performed to evaluate the functionality of the payload release and deployment mechanism. This included testing the ability of the retaining system to release the payload sled as well as the ability of the deployment charges to push the sled out of the payload bay in the nosecone. These tests were performed with half the number of charges that will be flown, in order to produce a conservative result and validate the dual redundancy on all release and deployment mechanisms. In this case, one line cutter was used to release the sled from the retaining lines, and one 20 g CO_2 cartridge was used to deploy the sled from the nosecone.

Figure 1.20: Full payload release and deployment test

1.5.2 Truck Testing

The purpose of truck testing is to evaluate the performance of the SRAD parachute. This includes validating inflation of the parachute and characterizing its drag coefficient in lieu of a launch. The tests were performed by attaching a parachute to the bed of a truck with the use of a truck testing rig and driving the truck as a predetermined speed. Four truck tests were performed, driving into and out of the wind at different velocities. Air velocity was measured using an anemometer attached to the truck, and force produced by the parachute was measured using a load cell.

Shown in Table 1.1 are the calculated drag coefficients for each of the four truck tests and their corresponding wind speeds, calculated using Equation 1.7. The design speed of the main chute was approximately 30 km/h and the design C_d was 0.80. The average of the four calculated C_d values was 0.647, which was lower than the design C_d. This was acceptable, as flying the chute in the wake of the truck reduced the effective canopy area and decreased the apparent force produced by the chute [14].

	60 km/h	30 km/h
Test 1	0.717	0.725
Test 2	0.533	0.614

Table 1.1: Calculated drag coefficients of truck tests

1.5.3 Test Flight

The entirety of the payload recovery system was tested during the test flight in May of 2025. This collected essential data regarding behaviour of the recovery system, including data on peak loads, nose cone free fall dynamics, parachute characterization, and retainment/deployment system reliability. Figure 1.21 shows the collective recovery system just prior to final assembly. This system weighed 16.2 lb, with the Cg sitting at 11.5 in from the base of the nosecone coupler.

Figure 1.21: Collective payload recovery system

First, the rotational frequency was determined to be around 1 Hz based on the lateral and axial acceleration data collected by the Raven2 altimeter. Oscillations can be observed in both acceleration graphs as the nosecone rotates into and out of the wind.

Then the terminal velocities were calculated for each stage of descent. This was done by using Equation 1.6 and the altitude-time data produced by a Raven2 altimeter (Figure 1.23). Note that this method is only applicable to stages of descent in which the descent velocity is approximately constant.

$$V_e = \frac{\Delta h}{\Delta t} \tag{1.6}$$

Where

V_e = terminal velocity
h = altitude
t = time in seconds

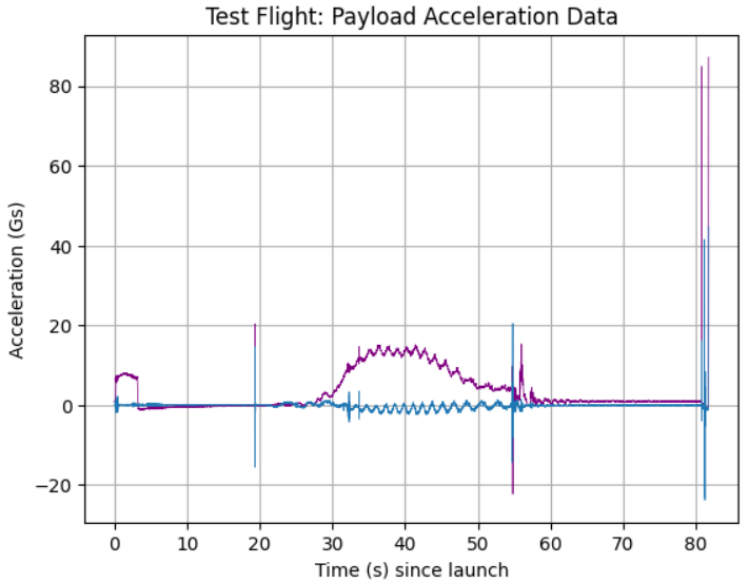

Figure 1.22: Payload testflight axial (purple) and lateral acceleration (blue)

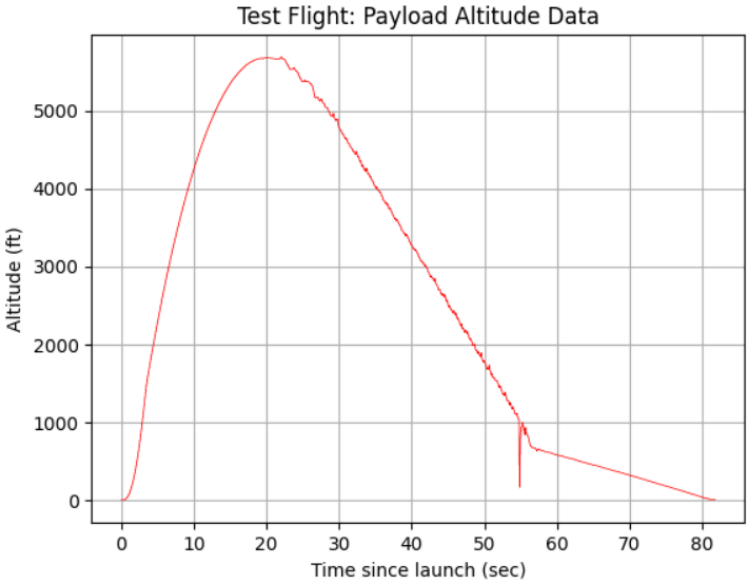

Figure 1.23: Payload altitude-time graph of the test flight

The general drag equation, provided by Knacke [14] is as follows.

$$F_d = \frac{1}{2} \cdot \rho \cdot v^2 \cdot C_d \cdot A \tag{1.7}$$

Where: F_d = drag force
ρ = density of air
v = velocity of rocket
C_d = drag coefficient
A = reference area

Equation 1.7 can be rearranged to solve for C_d.

$$C_d = \frac{2 \cdot F_d}{V_e^2 \cdot \rho \cdot A}$$

At 3000 ft, $\rho = 0.00218$ slugs/ft^3 and at 1000 ft, $\rho = 0.002377$ slugs/ft^3 [14].

For flat spin descent, approximating the cone as a flat triangle with $A = \frac{0.333 \text{ ft} \cdot 3.333 \text{ ft}}{2} = 0.556$ ft^2, calculations are as follows.

$$V_e = \frac{4776.39 - 1772.9}{30 - 50} = -150.17 \text{ ft/s}$$

$$C_d = \frac{2 \cdot 16.2}{150.17^2 \cdot 0.00218 \cdot 0.556} = 1.19$$

It is important to note that this C_d should only be applied if the profile and stability of the nosecone is identical to that of the one flown in the test flight.

For the main descent under the SRAD cross parachute, calculations were as follows.

$$V_e = \frac{576.2 - 35.88}{60 - 80} = -27.03 \text{ ft/s}$$

$$C_d = \frac{2 \cdot 16.2}{27.03^2 \cdot 0.002377 \cdot 23.44} = 0.796$$

Notably, the calculated main descent rate from the test flight was 99.78% accurate to the design value of 27.00 ft/s, and the main chute C_d was 99.5% accurate to the design value of 0.80.

REFERENCES

[1] S F Johnson. “The Evolution of FTIR Technology”. In: *ChemInform* 21 (44 Oct. 1990).

[2] A W Khan. *Physical Optics: Michelsons Interferometer*. June 2011.

[3] S J Ling, J Sanny, and W Moebs. *University Physics 3*. OpenStax. Sept. 2016.

[4] V Saptari. *Fourier-transform Spectroscopy Instrumentation Engineering*. SPIE Optical Engineering Press, 2004.

[5] P Heckbert. *Fourier Transforms and the Fast Fourier Transform (FFT) Algorithm*. Feb. 1995.

[6] *IR Spectrum of Nitrous Oxide*. NIST. 2018.

[7] *Calcium Fluoride Broadband Plate Beamsplitters for the Mid-IR*. ThorLabs.

[8] *Calcium Fluoride Windows*. ThorLabs.

[9] *Protected Gold Mirrors*. ThorLabs.

[10] *Calcium Fluoride Plano-Convex Lenses, AR Coated: 2-5ţm*. ThorLabs.

[11] P Yoder. *Mounting Optics in Optical Instruments*. SPIE Optical Engineering Press, 2002.

[12] Waterloo Rocketry. *Launch Canada 2025 Challenge: Final Design Report for Aurora*. Tech. rep. University of Waterloo, 2025.

[13] B. Ian Ruiz et al. *The Atmospheric Refractive Index Sounding Rockets Mission*. Tech. rep. University of Arizona Fairbanks, 1995. URL: https://ntrs.nasa.gov/api/citations/19960017260/downloads/19960017260.pdf.

[14] T.W. Knacke. *Parachute Recovery Systems: Design Manual*. Para Pub., 1992. ISBN: 9780915516858. URL: https://books.google.ca/books?id=5pzgAAAAMAAJ.

[15] Robert Gutenkauf R.J. Niccum E. L. Haak. *Drag and Stability of Cross Type Parachutes*. Tech. rep. University of Minnesota, 1965. URL: https://apps.dtic.mil/sti/tr/pdf/AD0460890.pdf.